**Nichlas Z. Swinteck**[1]
Postdoctoral Research Associate
e-mail: swinteck@email.arizona.edu

**Krishna Muralidharan**
Assistant Professor

**Pierre A. Deymier**
Professor

Department of Materials Science
and Engineering,
University of Arizona,
Tucson, AZ 85721

# Phonon Scattering in One-Dimensional Anharmonic Crystals and Superlattices: Analytical and Numerical Study

*Second-order perturbation theory based on multiple time scale analysis is used to illuminate three-phonon scattering processes in the one-dimensional anharmonic monoatomic crystal. Molecular dynamics simulation techniques in conjunction with spectral energy density analyses are used to quantify phonon mode lifetime in (1) the monoatomic crystal and (2) a series of superlattice configurations. It is found that the lifetime of vibrational modes in the monoatomic crystal is inherently long, because the conditions for conservation of wave vector and frequency are pathologically difficult to satisfy. Superlattice configurations, however, offer band-folding effects, whereby the availability of phonon decay channels decreases the lifetime of the vibrational modes supported by the medium.*
[DOI: 10.1115/1.4023824]

## 1 Introduction

The modes of vibration supported by harmonic crystals are noninteracting and propagate without decay. Anharmonic crystals allow vibrational modes to exchange energy via phonon decay channels when the conditions for conservation of momentum and energy are satisfied by the phonons involved in the scattering process. The study of multiphonon processes in nonlinear crystals has received considerable attention over the years. Anharmonic lattice dynamics methods have been applied to introduce phonon interactions in three-dimensional crystals as perturbations to the harmonic solution [1–3]. Nonlinear interatomic forces lead to mode-dependent frequency shifts and introduce finite phonon lifetime (i.e., line-width). Other approaches, such as diagrammatic techniques [4], thermodynamic Green's function methods [5], and multiple time scale perturbation expansion analyses [6,7] yield similar results to lattice dynamics. It is important to understand the effect nonlinear interatomic forces have on thermal phonon scattering processes for the design of efficient thermal interface materials and thermoelectric devices. Nanofabrication techniques can be used to structure matter in a way that affects the propagation characteristics of thermal phonons. Modulating the thermal properties of materials by creating a nanoscale composite structure is an approach that has been extensively studied in the case of superlattices [8–10]. These stacks of nanoscale layers have been shown experimentally [11] and theoretically [12] to impact thermal transport due to scattering effects of phonons. While superlattices are actually one-dimensional phononic structures, only a few studies have investigated two-dimensional (2D) and three-dimensional (3D) nanophononic structures. Most studies on 2D and 3D phononic crystals (PCs) have focused on macroscopic elastic systems. This large body of knowledge suggests a possibility of designing dispersive properties by downscaling PCs to nanodimensions to affect the propagation characteristics of phonons with frequencies exceeding the THz range [13]. Recently, Gillet et al. [14] have reported simulations of atomic-level phononic structures made of three-dimensional lattices of Ge quantum dots in a Si matrix. They have shown a decrease of thermal conductivity by several orders of magnitude due to the periodic structure of the system. Davis and Hussein [15] have considered three-dimensional nanoscale phononic crystals formed from silicon and cubic voids of vacuum. The voids are arranged on a simple cubic lattice with a lattice constant an order of magnitude larger than that of the bulk crystalline silicon primitive cell. This study showed that dispersion at the phononic crystal unit cell level plays a noticeable role in determining the thermal conductivity and that boundary scattering can also be a dominant factor. Control of high-frequency thermal phonons via structural periodicity requires preserving elastic Bragg scattering and is a significant challenge because of the possible loss of phonon coherence due to inherent inelastic scattering resulting from the anharmonicity of interatomic bonds.

In this study, a model comprised of a chain of masses and springs with nonlinear quadratic forces is considered to illuminate the effect of nonlinear interatomic forces on the vibrational modes supported by this medium. Amplitude-dependent self-interaction of a wave in a monoatomic and diatomic chain of masses and springs with nonlinear cubic forces has been studied [16]. It was shown that the dispersion curves undergo frequency shifts dependent on the amplitude of the wave. The interaction between two different waves in a nonlinear monoatomic chain results in the formation of different dispersion branches that are amplitude and frequency dependent [17]. In the present paper, second-order perturbation theory based on multiple time scale perturbation expansion analysis [6,7] is utilized to assess single wave interactions (self-interaction) and three-phonon processes in the 1D crystal model. A detailed derivation of the anharmonic modes for single-wave interactions and multiwave interactions is provided in Sec. 2. In Sec. 3.2, numerical affirmations of the expressions derived in Sec. 2 are presented via molecular dynamics (MD) simulations of the 1D nonlinear model. Section 3.3 extends MD simulation techniques to several superlattice configurations of the 1D model to illuminate phonon scattering mechanisms observed in periodic composite structures.

## 2 Analytical Analysis of 1D Anharmonic Monoatomic Crystal

A schematic illustration of the 1D monoatomic crystal is shown in Fig. 1(*a*). The potential energy function detailing the interaction between neighboring masses in the 1D crystal is shown in Fig. 1(*b*). The parameter ($\varepsilon$), characterizes the strength of nonlinearity in the springs connecting the masses. As $\varepsilon$ increases in magnitude, a region of instability emerges in the potential energy function. The equation of motion for the quadratically nonlinear monoatomic chain is represented by Eq. (1),

[1]Corresponding author.

Contributed by the Design Engineering Division of ASME for publication in the JOURNAL OF VIBRATION AND ACOUSTICS. Manuscript received April 29, 2012; final manuscript received October 22, 2013; published online June 6, 2013. Assoc. Editor: Michael Leamy.

  

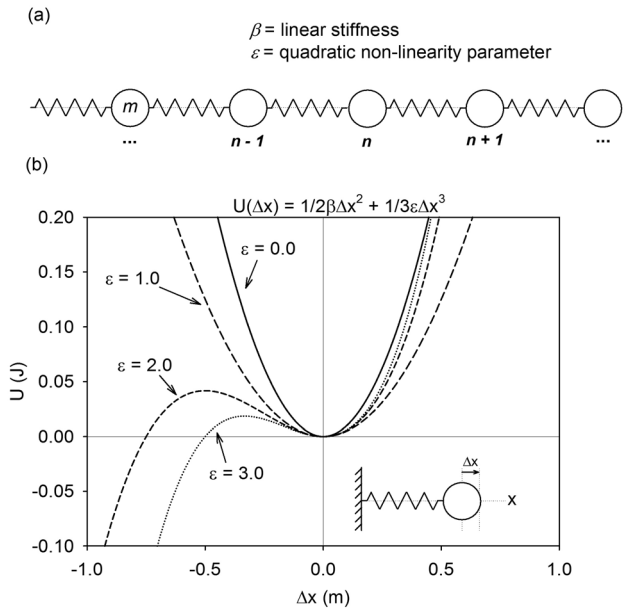


**Fig. 1 (*a*) Schematic representation of 1D crystal with linear stiffness $\beta$ and quadratic nonlinearity parameter $\varepsilon$. (*b*) The potential energy function describing the 1D crystal.**

$$m\frac{d^2u_n(t)}{dt^2} = \beta(u_{n+1} - 2u_n + u_{n-1}) + \varepsilon[(u_{n+1} - u_n)^2 - (u_n - u_{n-1})^2] \tag{1}$$

where $m$ is mass, $u_n(t)$ is the displacement from equilibrium of the $n$th mass, $\beta$ is linear stiffness, and $\varepsilon$ is a small parameter characterizing quadratic nonlinearity. The time variable ($t$) is replaced by a collection of variables $\tau = (\tau_0, \tau_1, \tau_2)$, whereby $\tau_0 = t$, $\tau_1 = \varepsilon t$, and $\tau_2 = \varepsilon^2 t$. Under this condition, Eq. (1) becomes

$$\frac{d^2u_n(\tau_0,\tau_1,\tau_2)}{dt^2} = \omega_n^2(u_{n+1} - 2u_n + u_{n-1}) + \frac{\varepsilon}{m}[(u_{n+1} - u_n)^2 - (u_n - u_{n-1})^2] \tag{2}$$

where $\omega_n = \sqrt{\beta/m}$.

The dependent variable in Eq. (2), $u_n(\tau)$, is expressed as an asymptotic expansion at multiple time scales,

$$u_n(\tau) = u_n^{(0)}(\tau) + \varepsilon u_n^{(1)}(\tau) + \varepsilon^2 u_n^{(2)}(\tau) + \text{higher order terms} \tag{3}$$

With this, Eq. (2) is decomposed into equations for each order of expansion of $\varepsilon$, namely, the following set of equations:

$$\mathrm{O}(\varepsilon^0): \frac{\partial^2 u_n^{(0)}}{\partial\tau_0^2} = \omega_n^2\left(u_{n+1}^{(0)} - 2u_n^{(0)} + u_{n-1}^{(0)}\right) \tag{4}$$

$$\mathrm{O}(\varepsilon^1): \frac{\partial^2 u_n^{(1)}}{\partial\tau_0^2} + 2\frac{\partial^2 u_n^{(0)}}{\partial\tau_0\partial\tau_1} = \omega_n^2\left(u_{n+1}^{(1)} - 2u_n^{(1)} + u_{n-1}^{(1)}\right) + \frac{1}{m}\left[u_{n+1}^{(0)}u_{n+1}^{(0)} - 2u_{n+1}^{(0)}u_n^{(0)} + 2u_{n-1}^{(0)}u_n^{(0)} - u_{n-1}^{(0)}u_{n-1}^{(0)}\right] \tag{5}$$

$$\mathrm{O}(\varepsilon^2): \frac{\partial^2 u_n^{(2)}}{\partial\tau_0^2} + 2\frac{\partial^2 u_n^{(1)}}{\partial\tau_0\partial\tau_1} + 2\frac{\partial^2 u_n^{(0)}}{\partial\tau_0\partial\tau_2} + \frac{\partial^2 u_n^{(0)}}{\partial\tau_1^2} = \omega_n^2\left(u_{n+1}^{(2)} - 2u_n^{(2)} + u_{n-1}^{(2)}\right) + \frac{2}{m}\left[u_{n+1}^{(1)}u_{n+1}^{(0)} - u_{n+1}^{(1)}u_n^{(0)} - u_{n+1}^{(0)}u_n^{(1)} + u_{n-1}^{(1)}u_n^{(0)} + u_{n-1}^{(0)}u_n^{(1)} - u_{n-1}^{(1)}u_{n-1}^{(0)}\right] \tag{6}$$

**2.1 Self-Interaction.** We first address the self-interaction of a vibrational mode—the effect of the lattice deformation on itself. To solve the $\varepsilon^0$ equation (Eq. (4)), a general solution of the following form is proposed:

$$u_{n,G}^{(0)}(\tau_0,\tau_1,\tau_2) = A_0(\tau_1,\tau_2)e^{ikna}e^{-i\omega_0\tau_0} + \bar{A}_0(\tau_1,\tau_2)e^{-ikna}e^{i\omega_0\tau_0} \tag{7}$$

where

$$A_0(\tau_1,\tau_2) = \alpha(\tau_1,\tau_2)e^{-i\varphi(\tau_1,\tau_2)}$$
$$\bar{A}_0(\tau_1,\tau_2) = \alpha(\tau_1,\tau_2)e^{-i\varphi(\tau_1,\tau_2)}$$

$A_0(\tau_1,\tau_2)$ is a complex quantity that permits slow time evolution of amplitude and phase and $\alpha(\tau_1,\tau_2)$ and $\varphi(\tau_1,\tau_2)$ are real-valued functions. Inserting Eqs. (7) into (4) yields the well-known dispersion relationship for the harmonic system Eq. (8),

$$\omega_0^2 = \omega_n^2(2 - e^{ika} - e^{-ika}) = \frac{\beta}{m}[2 - 2\cos(ka)] \tag{8}$$

Equation (7) is now utilized in the $\varepsilon^1$-order equation (Eq. (5)) to resolve the general solution for $u_n^{(1)}$. The $\varepsilon^1$-order equation is rewritten as follows:

$$\mathrm{O}(\varepsilon^1): \frac{\partial^2 u_n^{(1)}}{\partial\tau_0^2} + \omega_n^2\left(2u_n^{(1)} - u_{n+1}^{(1)} - u_{n-1}^{(1)}\right) = 2i\omega_0\left[\frac{\partial A_0}{\partial\tau_1}e^{ikna}e^{-i\omega_0\tau_0} - \frac{\partial\bar{A}_0}{\partial\tau_1}e^{-ikna}e^{i\omega_0\tau_0}\right] + \frac{1}{m}[(e^{i2ka} - 2e^{ika} + 2e^{-ika} - e^{-i2ka}) \times (A_0A_0e^{i2kna}e^{-i2\omega_0\tau_0} - \bar{A}_0\bar{A}_0e^{-i2kna}e^{i2\omega_0\tau_0})] \tag{9}$$

It is assumed that the solution to the homogeneous equation of Eq. (9) takes similar form to the general solution of Eq. (4). Under this assumption, terms on the right-hand side (RHS) of the Eq. (9) with functional form $e^{i\omega_0\tau_0}$ or $e^{-i\omega_0\tau_0}$ contribute to secular behavior. These terms are eliminated by setting them equal to zero. Accordingly, $A_0$ and $\bar{A}_0$ are considered to be independent functions of $\tau_1$. This modifies the form of the general solution to Eq. (4),

$$u_{n,G}^{(0)}(\tau_0,\tau_2) = A_0(\tau_2)e^{ikna}e^{-i\omega_0\tau_0} + \bar{A}_0(\tau_2)e^{-ikna}e^{i\omega_0\tau_0} \tag{10}$$

where

$$A_0(\tau_2) = \alpha(\tau_2)e^{-i\varphi(\tau_2)}$$
$$\bar{A}_0(\tau_2) = \alpha(\tau_2)e^{i\varphi(\tau_2)}$$

The homogeneous solution to Eq. (9) takes the following form:

$$u_{n,H}^{(1)}(\tau_0,\tau_2) = B_0(\tau_2)e^{ikna}e^{-i\omega_0\tau_0} + \bar{B}_0(\tau_2)e^{-ikna}e^{i\omega_0\tau_0} \tag{11}$$

The particular solution to Eq. (9) is of the form

$$u_{n,P}^{(1)}(\tau_0,\tau_2) = C_0(\tau_2)e^{i2kna}e^{-i2\omega_0\tau_0} + \bar{C}_0(\tau_2)e^{-i2kna}e^{i2\omega_0\tau_0} \tag{12}$$

Inserting Eq. (12) into Eq. (9) and relating like terms reveals relationships for the exponential prefactors $C_0(\tau_2)$ and $\bar{C}_0(\tau_2)$. Equation (12) becomes

$$u_{n,P}^{(1)}(\tau_0,\tau_2) = \frac{2i(\sin(2ka) - 2\sin(ka))}{\beta((2 - 2\cos(2ka)) - 4(2 - 2\cos(ka)))} \times \left[A_0^2e^{i2kna}e^{-i2\omega_0\tau_0} - \bar{A}_0^2e^{-i2kna}e^{i2\omega_0\tau_0}\right] \tag{13}$$

The general solution to Eq. (9) is a sum of the homogeneous ($u_{n,H}^{(1)}$) and particular solutions ($u_{n,P}^{(1)}$),

$$u_{n,G}^{(1)}(\tau_0,\tau_2) = B_0 e^{ikna} e^{-i\omega_0\tau_0} + \bar{B}_0 e^{-ikna} e^{i\omega_0\tau_0} + \frac{2i(\sin(2ka) - 2\sin(ka))}{\beta((2-2\cos(2ka)) - 4(2-2\cos(ka)))} \times [A_0 A_0 e^{i2kna} e^{-i2\omega_0\tau_0} - \bar{A}_0 \bar{A}_0 e^{-i2kna} e^{i2\omega_0\tau_0}] \quad (14)$$

The values for $B_0$ and $\bar{B}_0$ are found from initial conditions. With the general solutions to the $\varepsilon^0$-equation and the $\varepsilon^1$-equation, the $\varepsilon^2$-order equation is developed. Inserting Eq. (10) and Eq. (14) into Eq. (6), utilizing the expressions for $A_0(\tau_2)$ and $\bar{A}_0(\tau_2)$, and noting that $u_{n,G}^{(0)}$ and $u_{n,G}^{(1)}$ are independent functions of $\tau_1$, the $\varepsilon^2$-order equation is rewritten as

$$\mathrm{O}(\varepsilon^2): \frac{\partial^2 u_n^{(2)}}{\partial \tau_0^2} + \omega_n^2\left(2u_n^{(2)} - u_{n+1}^{(2)} - u_{n-1}^{(2)}\right) = e^{ikna} e^{-i\omega_0\tau_0}\left(2\omega_0\alpha\frac{\partial\varphi}{\partial\tau_2}e^{-i\varphi} + 2i\omega_0 e^{-i\varphi}\frac{\partial\alpha}{\partial\tau_2}\right) + e^{-ikna} e^{i\omega_0\tau_0}\left(2\omega_0\alpha\frac{\partial\varphi}{\partial\tau_2}e^{i\varphi} - 2i\omega_0 e^{i\varphi}\frac{\partial\alpha}{\partial\tau_2}\right) + \frac{2}{m}\{[(e^{i2ka} - 2e^{ika} + 2e^{-ika} - e^{-i2ka})(A_0 B_0 e^{i2kna} e^{-i2\omega_0\tau_0} - \bar{A}_0\bar{B}_0 e^{-i2kna} e^{i2\omega_0\tau_0})] + [(e^{i3ka} - e^{i2ka} - e^{ika} + e^{-ika} + e^{-i2ka} - e^{-i3ka})(A_0 C_0 e^{i3kna} e^{-i3\omega_0\tau_0} - \bar{A}_0\bar{C}_0 e^{-i3kna} e^{i3\omega_0\tau_0})] + [(e^{i2ka} - 2e^{ika} + 2e^{-ika} - e^{-i2ka})(A_0\bar{C}_0 e^{-ikna} e^{i\omega_0\tau_0} - \bar{A}_0 C_0 e^{ikna} e^{-i\omega_0\tau_0})]\} \quad (15)$$

The homogeneous solution to Eq. (15) is similar in form to the general solution of Eq. (4) and the homogeneous solution of Eq. (9). Accordingly, terms on the RHS of Eq. (15) with functional form $e^{i\omega_0\tau_0}$ or $e^{-i\omega_0\tau_0}$ contribute to secular behavior and must be eliminated. Setting exponential prefactors equal to zero yields the following relationships for $\alpha(\tau_2)$ and $\varphi(\tau_2)$:

$$\alpha(\tau_2) = \alpha_0 \quad (16)$$

$$\varphi(\tau_2) = -\frac{\alpha^2}{\omega_0\beta m}\cdot\frac{4(\sin(2ka) - 2\sin(ka))^2}{(2-2\cos(2ka)) - 4(2-2\cos(ka))}\tau_2 + \varphi_0 \quad (17)$$

where $\alpha_0$ and $\varphi_0$ are constants determined from initial plane wave conditions. The general solution to the $\varepsilon^0$ equation (Eq. (10)) is considered again with Eq. (16) and Eq. (17) substituted in for expressions $A_0$ and $\bar{A}_0$. Here, the constant $\varphi_0$ can be set equal to zero without loss of generality.

$$u_{n,G}^{(0)}(\tau_0,\tau_2) = \alpha_0 e^{i\left(kna - \left(\omega_0 - \varepsilon^2(\alpha^2/\omega_0\beta m)\cdot(4(\sin(2ka) - 2\sin(ka))^2/(2-2\cos(2ka)) - 4(2-2\cos(ka)))\right)\tau_0\right)} + \alpha_0 e^{-i\left(kna - \left(\omega_0 - \varepsilon^2(\alpha^2/\omega_0\beta m)\cdot(4(\sin(2ka) - 2\sin(ka))^2/(2-2\cos(2ka)) - 4(2-2\cos(ka)))\right)\tau_0\right)} \quad (18)$$

Equation (18) shows that the 0th order term in the asymptotic expansion of $u_n$ shows the harmonic dispersion curve is shifted by a quantity that has quadratic dependence on the strength of the nonlinearity parameter $\varepsilon$.

**2.2 Three-Wave Interactions.** Here, we consider the interaction between three waves with different wave vectors and frequencies. The analysis begins with the equation of motion (Eq. (1)) from Sec. 2.1. The displacement of the $n$th mass is represented by a superposition of wave modes, each with a unique time and wave vector-dependent amplitude factor (Eq. (19)),

$$u_n(t) = \Sigma_k A(k,t) e^{ikna} \quad (19)$$

Here, we use a discrete summation over the wave numbers instead of an integral over a continuum of wave vectors. This is done to help the reader conceptualize the interactions between specific phonons and to facilitate the comparison with the MD models presented subsequently (Sec. 3.2). Indeed, MD simulations are limited to finite size systems, for which the phonon modes do not form a continuum but a discrete set of possible wave vectors. Inserting Eq. (19) into the equation of motion for the 1D monoatomic crystal yields a modified equation of motion (Eq. (20)).

$$m\sum_k \frac{d^2A(k,t)}{dt^2}e^{ikna} = -4\beta\Sigma_k A(k,t)e^{ikna}\sin^2\left(\frac{ka}{2}\right) + \varepsilon[\Sigma_{k'}\Sigma_{k''}A(k',t)A(k'',t)e^{i(k'+k'')na}f(k',k'')] \quad (20)$$

where $f(k',k'') = -8i\sin(k'a/2)\sin(k''a/2)\sin((k'+k'')a/2)$. Equation (20) is multiplied by $e^{-ik^*na}$, and a summation over all $n$ masses is imposed. With $\omega_n^2 = 4\beta/m$, Eq. (20) becomes

$$\frac{d^2A(k^*,t)}{dt^2} + \omega_n^2\sin^2\left(\frac{k^*a}{2}\right)A(k^*,t) = \frac{\varepsilon}{m}\Sigma_{k'}\Sigma_{k''}A(k',t)A(k'',t)f(k',k'')\delta_{k'+k'',k^*} \quad (21)$$

$\delta_{k'+k'',k^*}$ imposes the wave vector conservation rule $k^* = k' + k'' + mG$, where $m$ is an integer and $G$ is a reciprocal lattice vector of the periodic structure. We do not label $G$ in the delta function for the sake of simplicity of the notation. For $m = 0$, one has the so-called normal three phonon scattering process. The case of $m \neq 0$ corresponds to umklapp processes, where $k' + k''$ is located outside the first Brillouin zone. In Eq. (21), the variable $\tau$ is introduced, where $\tau = \omega_n t$. Single time variables ($\tau$) are replaced by a collection of variables $\tau = (\tau_0, \tau_1, \tau_2)$, whereby $\tau_0 = \tau$, $\tau_1 = \varepsilon\tau$, and $\tau_2 = \varepsilon^2\tau$. Additionally, $A(k^*, \tau)$ is replaced by an asymptotic expansion, whereby

$$A(k^*,\tau) = A_0(k^*,\tau) + \varepsilon A_1(k^*,\tau) + \varepsilon^2 A_2(k^*,\tau)$$

$$A(k^*,\tau_0,\tau_1,\tau_2) = A_0(k^*,\tau_0,\tau_1,\tau_2) + \varepsilon A_1(k^*,\tau_0,\tau_1,\tau_2) + \varepsilon^2 A_2(k^*,\tau_0,\tau_1,\tau_2)$$

With these considerations, Eq. (21) is separated into expressions at order $\varepsilon^0$, $\varepsilon^1$, and $\varepsilon^2$,

$$O(\varepsilon^0): \frac{\partial^2 A_0(k^*,\tau)}{\partial \tau_0^2} + \sin^2\left(\frac{k^* a}{2}\right) A_0(k^*,\tau) = 0 \tag{22}$$

$$O(\varepsilon^1): \frac{\partial^2 A_1(k^*,\tau)}{\partial \tau_0^2} + 2\frac{\partial^2 A_0(k^*,\tau)}{\partial \tau_1 \partial \tau_0} + \sin^2\left(\frac{k^* a}{2}\right) A_1(k^*,\tau)$$
$$= \frac{1}{m\omega_n^2} \Sigma_{k'} \Sigma_{k''} f(k',k'') \delta_{k'+k'',k^*} [A_0(k',\tau) A_0(k'',\tau)] \tag{23}$$

$$O(\varepsilon^2): \frac{\partial^2 A_2(k^*,\tau)}{\partial \tau_0^2} + 2\frac{\partial^2 A_1(k^*,\tau)}{\partial \tau_1 \partial \tau_0} + 2\frac{\partial^2 A_0(k^*,\tau)}{\partial \tau_2 \partial \tau_0} + \frac{\partial^2 A_0(k^*,\tau)}{\partial \tau_1^2}$$
$$+ \sin^2\left(\frac{k^* a}{2}\right) A_2(k^*,\tau) = \frac{1}{m\omega_n^2} \Sigma_{k'} \Sigma_{k''} f(k',k'') \delta_{k'+k'',k^*}$$
$$\times [A_0(k',\tau) A_1(k'',\tau) + A_1(k',\tau) A_0(k'',\tau)] \tag{24}$$

To solve Eq. (22), a general solution of the following form is proposed:

$$A_0(k^*,\tau_0,\tau_1,\tau_2) = a_0(k^*,\tau_1,\tau_2) e^{i\omega_0^* \tau_0} + \bar{a}_0(k^*,\tau_1,\tau_2) e^{-i\omega_0^* \tau_0} \tag{25}$$

Inserting Eq. (25) into Eq. (22) offers the expected relationship between $\omega_0^*$ and $k^*$: $\omega_0^{*2} = \sin^2(k^* a/2)$. Inserting Eq. (25) into Eq. (23) offers an expression to solve for $A_1(k^*,\tau)$. After rearranging and utilizing the following definitions:

$$A_0(k',\tau_0,\tau_1,\tau_2) = a_0(k',\tau_1,\tau_2) e^{i\omega_0' \tau_0} + \bar{a}_0(k',\tau_1,\tau_2) e^{-i\omega_0' \tau_0}$$

$$A_0(k'',\tau_0,\tau_1,\tau_2) = a_0(k'',\tau_1,\tau_2) e^{i\omega_0'' \tau_0} + \bar{a}_0(k',\tau_1,\tau_2) e^{-i\omega_0'' \tau_0}$$

the $\varepsilon^1$ equation becomes

$$O(\varepsilon^1): \frac{\partial^2 A_1(k^*,\tau)}{\partial \tau_0^2} + \omega_0^{*2} A_1(k^*,\tau)$$
$$= -2i\omega_0^* \left[\frac{\partial a_0^*}{\partial \tau_1} e^{i\omega_0^* \tau_0} - \frac{\partial \bar{a}_0^*}{\partial \tau_1} e^{-i\omega_0^* \tau_0}\right] + \frac{1}{m\omega_n^2} \sum_{k'} \sum_{k''} f(k',k'') \delta_{k'+k'',k^*}$$
$$\times [a_0' a_0'' e^{i(\omega_0' + \omega_0'')\tau_0} + a_0' \bar{a}_0'' e^{i(\omega_0' + \omega_0'')\tau_0}$$
$$+ \bar{a}_0' a_0'' e^{-i(\omega_0' - \omega_0'')\tau_0} + \bar{a}_0' \bar{a}_0'' e^{-i(\omega_0' + \omega_0'')\tau_0}] \tag{26}$$

where terms like $a_0^*, a_0', a_0''$…etc. are compact representations for $a_0(k^*,\tau_1,\tau_2), a_0(k',\tau_1,\tau_2), a_0(k'',\tau_1,\tau_2), \ldots$, etc. A homogeneous solution to Eq. (26) is proposed,

$$A_{1,H}(k^*,\tau_0,\tau_2) = a_1(k^*,\tau_2) e^{i\omega_0^* \tau_0} + \bar{a}_1(k^*,\tau_2) e^{-i\omega_0^* \tau_0}$$
$$= a_1^* e^{i\omega_0^* \tau_0} + \bar{a}_1^* e^{-i\omega_0^* \tau_0} \tag{27}$$

The forcing terms on the right-hand side (RHS) of Eq. (26) with functional form $e^{i\omega_0^* \tau_0}$ or $e^{-i\omega_0^* \tau_0}$ contribute to secular behavior. These terms must be eliminated such that the final representation of $A(k^*, \tau)$ is well behaved (e.g., contains no terms that temporally grow without bound). These terms are set to zero by making $a_0^*$ and $\bar{a}_0^*$ functions of $k^*$ and $\tau_2$ only. With this stipulation, an appropriate form of the particular solution to Eq. (26) is

$$A_{1,P}(k^*,\tau) = \frac{1}{m\omega_n^2} \Sigma_{k'} \Sigma_{k''} f(k',k'') \delta_{k'+k'',k^*} [b_1 e^{i(\omega_0' + \omega_0'')\tau_0}$$
$$+ \bar{b}_1 e^{-i(\omega_0' + \omega_0'')\tau_0} + c_1 e^{i(\omega_0' - \omega_0'')\tau_0} + \bar{c}_1 e^{-i(\omega_0' - \omega_0'')\tau_0}] \tag{28}$$

The exponential prefactors $b_1, \bar{b}_1, c_1, \bar{c}_1$ have dependency on $k', k'', \tau_2, \omega_0^*, \omega_0', \omega_0''$. Substituting Eq. (28) into Eq. (26) and relating like terms reveals the exponential prefactors: $b_1, \bar{b}_1, c_1, \bar{c}_1$

$$b_1 = \frac{a_0(k',\tau_2) a_0(k'',\tau_2)}{\omega_0^{*2} - (\omega_0' + \omega_0'')^2}; \quad \bar{b}_1 = \frac{\bar{a}_0(k',\tau_2) \bar{a}_0(k'',\tau_2)}{\omega_0^{*2} - (\omega_0' + \omega_0'')^2}$$

$$c_1 = \frac{a_0(k',\tau_2) \bar{a}_0(k'',\tau_2)}{\omega_0^{*2} - (\omega_0' - \omega_0'')^2}; \quad \bar{c}_1 = \frac{\bar{a}_0(k',\tau_2) a_0(k'',\tau_2)}{\omega_0^{*2} - (\omega_0' - \omega_0'')^2}$$

In the long wavelength limit, angular frequency has nearly linear dependence on wave vector. In considering the stipulated wave vector relationship inside the double summation in Eq. (28), $(k' + k'' = k^*)$, it is conceivable that $\omega_0(k') + \omega_0(k'') = \omega_0(k^*)$ or $\omega_0(k') - \omega_0(k'') = \omega_0(k^*)$. In this instance, the denominator terms in the expressions for $b_1, \bar{b}_1, c_1, \bar{c}_1$ will go to zero. To avoid this complication, following the procedure stipulated by Khoo and Wang [6], a small imaginary part $\varphi$ is introduced in the denominator. At the final result of the calculation, a limit will be taken as $\varphi \to 0$. The general solution to Eq. (26) is a sum of Eq. (27) and Eq. (28),

$$A_1(k^*,\tau_0,\tau_2) = a_1^* e^{i\omega_0^* \tau_0} + \bar{a}_1^* e^{-i\omega_0^* \tau_0} + \frac{1}{m\omega_n^2} \Sigma_{k'} \Sigma_{k''} f(k',k'') \delta_{k'+k'',k^*}$$
$$\times \left[\frac{a_0' a_0''}{g_1^*} e^{i(\omega_0' + \omega_0'')\tau_0} + \frac{\bar{a}_0' \bar{a}_0''}{g_1^*} e^{-i(\omega_0' + \omega_0'')\tau_0}\right.$$
$$\left. + \frac{\bar{a}_0' a_0''}{g_2^*} e^{i(\omega_0' - \omega_0'')\tau_0} + \frac{a_0' \bar{a}_0''}{g_2^*} e^{-i(\omega_0' - \omega_0'')\tau_0}\right] \tag{29}$$

where $g_1^* = \omega_0^{*2} - (\omega_0' + \omega_0'')^2 + i\varphi; g_2^* = \omega_0^{*2} - (\omega_0' - \omega_0'')^2 + i\varphi$. Equation (24) is reduced to the following expressions because $A_0(k^*,\tau)$ and $A_1(k^*,\tau)$ are independent of $\tau_1$:

$$O(\varepsilon^2): \frac{\partial^2 A_2(k^*,\tau_0,\tau_1,\tau_2)}{\partial \tau_0^2} + \omega_0^{*2} A_2(k^*,\tau_0,\tau_1,\tau_2)$$
$$= -2i\omega_0^* \frac{\partial a_0(k^*,\tau_2)}{\partial \tau_2} e^{i\omega_0^* \tau_0} + 2i\omega_0^* \frac{\partial \bar{a}_0(k^*,\tau_2)}{\partial \tau_2} e^{-i\omega_0^* \tau_0}$$
$$+ \frac{1}{m\omega_n^2} \sum_{k'} \sum_{k''} f(k',k'') \delta_{k'+k'',k^*} [A_0(k',\tau_0,\tau_2) A_1(k'',\tau_0,\tau_2)$$
$$+ A_1(k',\tau_0,\tau_2) A_0(k'',\tau_0,\tau_2)] \tag{30}$$

As before, the solution to the homogeneous equation of Eq. (30) is of the form

$$A_{2,H}(k^*,\tau_0,\tau_2) = a_2(k^*,\tau_2) e^{i\omega_0^* \tau_0} + \bar{a}_2(k^*,\tau_2) e^{-i\omega_0^* \tau_0} \tag{31}$$

Terms on the RHS of Eq. (30) with functional form $e^{i\omega_0^* \tau_0}$ or $e^{-i\omega_0^* \tau_0}$ contribute to secular behavior. Using Eqs. (25) and (29) to develop the RHS of Eq. (30) gives Eq. (32).

$$\frac{\partial^2 A_2(k^*,\tau_0,\tau_1,\tau_2)}{\partial\tau_0^2}+\omega_0^{*2}A_2(k^*,\tau_0,\tau_1,\tau_2)$$
$$=-2i\omega_0^*\frac{\partial a_0(k^*,\tau_2)}{\partial\tau_2}e^{i\omega_0^*\tau_0}+2i\omega_0^*\frac{\partial\bar{a}_0(k^*,\tau_2)}{\partial\tau_2}e^{-i\omega_0^*\tau_0}+\frac{1}{m\omega_n^2}\sum_{k'}\sum_{k''}f(k',k'')\partial_{k'+k'',k^*}$$
$$\times(a_0'a_1''e^{i(\omega_0'+\omega_0'')\tau_0}+a_0'\bar{a}_1''e^{i(\omega_0'-\omega_0'')\tau_0}+\bar{a}_0'a_1''e^{-i(\omega_0'-\omega_0'')\tau_0}+\bar{a}_0'\bar{a}_1''e^{-i(\omega_0'+\omega_0'')\tau_0})$$
$$+\frac{1}{m\omega_n^2}\sum_{k'}\sum_{k''}f(k',k'')\partial_{k'+k'',k^*}(a_0''a_1'e^{i(\omega_0''+\omega_0')\tau_0}+a_0''\bar{a}_1'e^{i(\omega_0''+\omega_0')\tau_0}+\bar{a}_0''a_1'e^{-i(\omega_0''-\omega_0')\tau_0}+\bar{a}_0''\bar{a}_1'e^{-i(\omega_0''+\omega_0')\tau_0})$$
$$+\frac{1}{m\omega_n^2}\Sigma_{k'}\Sigma_{k''}f(k',k'')\delta_{k'+k'',k^*}\left\{\left[\frac{1}{m\omega_n^2}\Sigma_{k_1}\Sigma_{k_2}f(k_1,k_2)\delta''_{k_1+k_2,k}\left[\frac{a_0'a_0^{(1)}a_0^{(2)}}{g_1''}e^{i(\omega_0^{(1)}+\omega_0^{(2)}+\omega_0')\tau_0}+\frac{a_0'\bar{a}_0^{(1)}\bar{a}_0^{(2)}}{g_1''}e^{-i(\omega_0^{(1)}-\omega_0^{(2)}-\omega_0')\tau_0}\right.\right.\right.$$
$$+\frac{a_0'a_0^{(1)}\bar{a}_0^{(2)}}{g_2''}e^{-i(\omega_0^{(1)}-\omega_0^{(2)}-\omega_0')\tau_0}+\frac{a_0'\bar{a}_0^{(1)}a_0^{(2)}}{g_2''}e^{-i(\omega_0^{(1)}-\omega_0^{(2)}-\omega_0')\tau_0}+\frac{\bar{a}_0'a_0^{(1)}a_0^{(2)}}{g_1''}e^{i(\omega_0^{(1)}+\omega_0^{(2)}-\omega_0')\tau_0}+\frac{\bar{a}_0'\bar{a}_0^{(1)}\bar{a}_0^{(2)}}{g_1''}e^{-i(\omega_0^{(1)}+\omega_0^{(2)}+\omega_0')\tau_0}$$
$$\left.\left.\left.+\frac{\bar{a}_0'a_0^{(1)}\bar{a}_0^{(2)}}{g_2''}e^{i(\omega_0^{(1)}-\omega_0^{(2)}-\omega_0')\tau_0}+\frac{\bar{a}_0'\bar{a}_0^{(1)}a_0^{(2)}}{g_2''}e^{-i(\omega_0^{(1)}-\omega_0^{(2)}+\omega_0')\tau_0}\right]\right]\right.$$
$$+\left[\frac{1}{m\omega_n^2}\Sigma_{k_1}\Sigma_{k_2}f(k_1,k_2)\delta'_{k_1+k_2,k}\left[\frac{a_0''a_0^{(1)}a_0^{(2)}}{g_1'}e^{i(\omega_0^{(1)}+\omega_0^{(2)}+\omega_0'')\tau_0}+\frac{a_0''\bar{a}_0^{(1)}\bar{a}_0^{(2)}}{g_1'}e^{-i(\omega_0^{(1)}+\omega_0^{(2)}-\omega_0'')\tau_0}+\frac{a_0''\bar{a}_0^{(1)}\bar{a}_0^{(2)}}{g_2'}e^{-i(\omega_0^{(1)}-\omega_0^{(2)}+\omega_0'')\tau_0}\right.\right.$$
$$+\frac{a_0''\bar{a}_0^{(1)}a_0^{(2)}}{g_2'}e^{-i(\omega_0^{(1)}-\omega_0^{(2)}-\omega_0'')\tau_0}+\frac{\bar{a}_0''a_0^{(1)}a_0^{(2)}}{g_1'}e^{i(\omega_0^{(1)}+\omega_0^{(2)}-\omega_0'')\tau_0}+\frac{\bar{a}_0''\bar{a}_0^{(1)}\bar{a}_0^{(2)}}{g_1'}e^{-i(\omega_0^{(1)}+\omega_0^{(2)}+\omega_0'')\tau_0}$$
$$\left.\left.+\frac{\bar{a}_0''a_0^{(1)}\bar{a}_0^{(2)}}{g_2'}e^{i(\omega_0^{(1)}-\omega_0^{(2)}-\omega_0'')\tau_0}+\frac{\bar{a}_0''\bar{a}_0^{(1)}a_0^{(2)}}{g_2'}e^{-i(\omega_0^{(1)}-\omega_0^{(2)}+\omega_0'')\tau_0}\right]\right]\right\} \tag{32}$$

There is notable similarity between the terms on the RHS of Eq. (26) that was solved to yield Eq. (29) and the third and fourth terms on the RHS of Eq. (32). The terms in Eq. (32) are treated with the same procedure; accordingly, they will not contribute to secular behavior. From here, the objective is to identify terms in Eq. (32) with $e^{i\omega_0^*\tau_0}$ or $e^{-i\omega_0^*\tau_0}$ dependency. This will be done by systematically evaluating wave vector pairs $\{k_1, k_2\}$ that satisfy the wave vector constraint stipulated by Eq. (32). Specifically,

$$\delta_{k'+k'',k^*}\delta_{k_1+k_2,k''}\rightarrow k'+k_1+k_2=k^*$$
$$\delta_{k'+k'',k^*}\delta_{k_1+k_2,k'}\rightarrow k''+k_1+k_2=k^*$$

If a certain pair of wave vectors satisfies the above-mentioned wave vector constraints, then an analysis will be carried through to see if these wave vectors give rise to terms with $e^{i\omega_0^*\tau_0}$ or $e^{-i\omega_0^*\tau_0}$ dependence. As before, terms with $e^{i\omega_0^*\tau_0}$ or $e^{-i\omega_0^*\tau_0}$ dependence will be removed.

In Eq. (32), inside the summation over $k'$, $k''$, there are two summations over $k_1$, $k_2$. For the first summation over $k_1$, $k_2$, two conditions must be met: (1) $k'+k''=k^*$ and (2) $k_1+k_2=k''$. The only possible combinations for $k_1$, $k_2$ that give wave vector relationships that are compatible with $\delta_{k'+k'',k^*}$ are shown as Condition A and Condition B:

Condition A: $k_1=-k'$, $k_2=k^*$, and $-k'+k^*=k''$
Condition B: $k_1=k^*$, $k_2=-k'$, and $k^*-k'=k''$

For the second summation over $k_1$, $k_2$, two conditions must be met: (1) $k'+k''=k^*$ and (2) $k_1+k_2=k'$. The only possible combinations for $k_1$, $k_2$ that give wave vector relationships that are compatible with $\delta_{k'+k'',k^*}$ are shown as Condition C and Condition D:

Condition C: $k_1=-k''$, $k_2=k^*$, and $-k''+k^*=k'$
Condition D: $k_1=k^*$, $k_2=-k''$, and $k^*-k''=k'$

Now that wave vector constraints are satisfied, an analysis is carried out to see if any terms with $e^{i\omega_0^*\tau_0}$ or $e^{-i\omega_0^*\tau_0}$ dependence arise. Explicitly, we only show the procedure to yield secular terms associated with Condition A. Similar treatment can reveal secular terms for Conditions B, C, and D. The following frequency relationships are present in the first summation over $k_1$, $k_2$ in Eq. (32):

(i) $\omega_0^{(1)}+\omega_0^{(2)}+\omega_0'$

(ii) $\omega_0^{(1)}+\omega_0^{(2)}-\omega_0'$

(iii) $\omega_0^{(1)}-\omega_0^{(2)}+\omega_0'$

(iv) $\omega_0^{(1)}-\omega_0^{(2)}-\omega_0'$

Applying Condition A to these frequency relationships shows two relationships that offer terms with $e^{i\omega_0^*\tau_0}$ or $e^{-i\omega_0^*\tau_0}$ dependence,

Condition A: $k_1=-k'\rightarrow\omega_0^{(1)}=\omega_0'$ and $k_2=k^*\rightarrow\omega_0^{(2)}=\omega_0^*$

Applying Condition A to frequency relationships leads to

(i) $\omega_0^{(1)}+\omega_0^{(2)}+\omega_0'\rightarrow\omega_0'+\omega_0^*+\omega_0'=\omega_0^*+2\omega_0'$

(ii) $\omega_0^{(1)}+\omega_0^{(2)}-\omega_0'\rightarrow\omega_0'+\omega_0^*-\omega_0'=\omega_0^*$

(iii) $\omega_0^{(1)}-\omega_0^{(2)}+\omega_0'\rightarrow\omega_0'-\omega_0^*+\omega_0'=-\omega_0^*+2\omega_0'$

(iv) $\omega_0^{(1)}-\omega_0^{(2)}-\omega_0'\rightarrow\omega_0'-\omega_0^*-\omega_0'=-\omega_0^*$

As a result, with Condition A, the following terms in the first summation over $k_1$, $k_2$ contribute to secular terms:

$$\frac{a_0'\bar{a}_0^{(1)}\bar{a}_0^{(2)}}{g_1''}e^{-i(\omega_0^{(1)}+\omega_0^{(2)}-\omega_0')\tau_0}=\frac{a_0'\bar{a}_0'\bar{a}_0^*}{g_1''}e^{-i(\omega_0'+\omega_0^*-\omega_0')\tau_0}$$
$$=\frac{a_0'\bar{a}_0'\bar{a}_0^*}{g_1''}e^{-i(\omega_0^*)\tau_0}$$

$$\frac{\bar{a}_0'a_0^{(1)}a_0^{(2)}}{g_1''}e^{i(\omega_0^{(1)}+\omega_0^{(2)}-\omega_0')\tau_0}=\frac{\bar{a}_0'a_0'a_0^*}{g_1''}e^{i(\omega_0'+\omega_0^*-\omega_0')\tau_0}$$
$$=\frac{\bar{a}_0'a_0'a_0^*}{g_1''}e^{i(\omega_0^*)\tau_0}$$

$$\frac{a_0' \bar{a}_0^{(1)} a_0^{(2)}}{g_2'' 2} e^{-i(\omega_0^{(1)} - \omega_0^{(2)} - \omega_0')\tau_0} = \frac{a_0' \bar{a}_0' \bar{a}_0^*}{g_2''} e^{-i(\omega_0' - \omega_0^* - \omega_0')\tau_0}$$

$$= \frac{a_0' \bar{a}_0^{(1)} a_0^{(2)}}{g_2''} e^{-i(\omega_0^*)\tau_0}$$

$$\frac{\bar{a}_0' a_0^{(1)} \bar{a}_0^{(2)}}{g_2''} e^{i(\omega_0^{(1)} - \omega_0^{(2)} - \omega_0')\tau_0} = \frac{\bar{a}_0' a_0' \bar{a}_0^*}{g_2''} e^{i(\omega_0' - \omega_0^* - \omega_0')\tau_0}$$

$$= \frac{\bar{a}_0' a_0^{(1)} \bar{a}_0^{(2)}}{g_2''} e^{-i(\omega_0^*)\tau_0}$$

In assuming that terms $[a_0(k'), \bar{a}_0(k'), a_0(-k'), \bar{a}_0(-k'), \ldots, \text{etc.}]$ in Eq. (32) behave as follows:

$$a_0(k', \tau_2) = a_0(k', 0) e^{i\beta(k')\tau_2}$$
$$\bar{a}_0(k', \tau_2) = \bar{a}_0(k', 0) e^{-i\beta(k')\tau_2}$$
$$a_0(-k', \tau_2) = a_0(-k', 0) e^{i\beta(-k')\tau_2}$$
$$\bar{a}_0(-k', \tau_2) = \bar{a}_0(-k', 0) e^{-i\beta(-k')\tau_2}$$
$$\vdots$$

etc.

additionally,

$$a_0(k', 0) = a_0(-k', 0)$$
$$\bar{a}_0(k', 0) = \bar{a}_0(-k', 0)$$
$$\beta(k') = \beta(-k')$$

Equation (32) can be rewritten in the form of Eq. (33),

$$\frac{\partial^2 A_2(k^*, \tau_0, \tau_1, \tau_2)}{\partial \tau_0^2} + \omega_0^{*2} A_2(k^*, \tau_0, \tau_1, \tau_2) = \left\{ -2i\omega_0^* \frac{\partial a_0(k^*, \tau_2)}{\partial \tau_2} + a_0(k^*, 0) e^{i\beta(k^*)\tau_2} \left(\frac{1}{m\omega_n^2}\right)^2 \sum_{k'} \sum_{k''} f(k', k'') \delta_{k'+k'', k^*} \right.$$
$$\times \left[ 2f(-k', k^*) \delta_{-k'+k^*, k''} a_0(k', 0) \bar{a}_0(k', 0) \left[ \frac{1}{g_1''} + \frac{1}{g_2''} \right] \right.$$
$$\left. \left. + 2f(-k'', k^*) \delta'_{-k''+k^*, k} a_0(k'', 0) \bar{a}_0(k'', 0) \left[ \frac{1}{g_1'} + \frac{1}{g_2'} \right] \right] \right\} e^{i\omega_0^* \tau_0}$$
$$+ \left\{ 2i\omega_0^* \frac{\partial \bar{a}_0(k^*, \tau_2)}{\partial \tau_2} + \bar{a}_0(k^*, 0) e^{-i\beta(k^*)\tau_2} \left(\frac{1}{m\omega_n^2}\right)^2 \sum_{k'} \sum_{k''} f(k', k'') \delta_{k'+k'', k^*} \right.$$
$$\times \left[ 2f(-k', k^*) \delta_{-k'+k^*, k''} a_0(k', 0) \bar{a}_0(k', 0) \left[ \frac{1}{g_1''} + \frac{1}{g_2''} \right] \right.$$
$$\left. \left. + 2f(-k'', k^*) \delta_{-k''+k^*, k'} a_0(k_0'', 0) \bar{a}_0(k'', 0) \left[ \frac{1}{g_1'} + \frac{1}{g_2'} \right] \right] \right\} e^{-i\omega_0^* \tau_0}$$
$$+ \text{other terms which will not give } e^{i\omega_0^* \tau_0} \text{ or } e^{-i\omega_0^* \tau_0} \tag{33}$$

where

$$g_1' = \omega_0'^2 - (\omega_0^* + \omega_0'')^2 + i\varphi; \quad g_2' = \omega_0'^2 - (\omega_0^* - \omega_0'')^2 + i\varphi$$

$$g_1'' = \omega_0''^2 - (\omega_0^* + \omega_0')^2 + i\varphi; \quad g_2'' = \omega_0''^2 - (\omega_0^* - \omega_0')^2 + i\varphi$$

The terms in front of $e^{i\omega_0^* \tau_0}$ and $e^{-i\omega_0^* \tau_0}$ are set to zero, and an expression for $\beta^*$ results (Eq. (34)),

$$\beta(k^*) = -\frac{1}{2\omega_0^*} \left(\frac{1}{m\omega_n^2}\right)^2 \Sigma_{k'} \Sigma_{k''} f(k', k'') \delta_{k'+k'', k^*}$$
$$\times \left[ 2f(-k', k^*) \delta_{-k'+k^*, k''} a_0(k', 0) \bar{a}_0(k', 0) \left[ \frac{1}{g_1''} + \frac{1}{g_2''} \right] \right.$$
$$\left. + 2f(-k'', k^*) \delta_{-k''+k^*, k'} a_0(k'', 0) \bar{a}_0(k'', 0) \left[ \frac{1}{g_1'} + \frac{1}{g_2'} \right] \right] \tag{34}$$

Recall that $\varphi$ appears in the terms containing $g_1'', g_2'', g_1', g_2'$. The limit of Eq. (34) is taken as $\varphi \to 0$. The following definition is utilized [6]:

$$\lim_{\theta \to 0} \frac{1}{(x \pm i\theta)} = \left(\frac{1}{x}\right)_{pp} \mp i\pi\delta(x)$$

where $pp$ denotes principle part. The real and imaginary parts of Eq. (34) are shown as Eqs. (35) and (36), respectively.

$$\text{Re}(\beta^*) = \Delta_{k^*} = \frac{-64}{\omega_0^*} \left(\frac{1}{m\omega_n^2}\right)^2 \Sigma_{k'} \Sigma_{k''} \sin^2\left(\frac{k'a}{2}\right) \sin^2\left(\frac{k''a}{2}\right) \sin^2\left(\frac{k^*a}{2}\right)$$
$$\times \left\{ a_0' \bar{a}_0' \left[ \left( \frac{1}{\omega_0''^2 - (\omega_0^* + \omega_0')^2} \right)_{pp} + \left( \frac{1}{\omega_0''^2 - (\omega_0^* - \omega_0')^2} \right)_{pp} \right] \right.$$
$$\left. + a_0'' \bar{a}_0'' \left[ \left( \frac{1}{\omega_0'^2 - (\omega_0^* + \omega_0'')^2} \right)_{pp} + \left( \frac{1}{\omega_0'^2 - (\omega_0^* - \omega_0'')^2} \right)_{pp} \right] \right\} \tag{35}$$

$$\text{Im}(\beta^*) = \Gamma_{k^*} = \frac{32\pi}{\omega_0^*} \left(\frac{1}{m\omega_n^2}\right)^2 \Sigma_{k'} \Sigma_{k''} \sin^2\left(\frac{k'a}{2}\right) \sin^2\left(\frac{k''a}{2}\right) \sin^2\left(\frac{k^*a}{2}\right)$$
$$\times \left\{ \delta(\omega_0^* + \omega_0' + \omega_0'') \left[ \frac{a_0' \bar{a}_0'}{\omega_0''} + \frac{a_0'' \bar{a}_0''}{\omega_0'} \right] \right.$$
$$- \delta(\omega_0^* + \omega_0' - \omega_0'') \left[ \frac{a_0' \bar{a}_0'}{\omega_0''} - \frac{a_0'' \bar{a}_0''}{\omega_0'} \right]$$
$$+ \delta(\omega_0^* - \omega_0' + \omega_0'') \left[ \frac{a_0' \bar{a}_0'}{\omega_0''} - \frac{a_0'' \bar{a}_0''}{\omega_0'} \right]$$
$$\left. - \delta(\omega_0^* - \omega_0' - \omega_0'') \left[ \frac{a_0' \bar{a}_0'}{\omega_0''} + \frac{a_0'' \bar{a}_0''}{\omega_0'} \right] \right\} \tag{36}$$

In the above expressions for the real and imaginary parts of $\beta^*$,

$$a_0'\bar{a}_0' = a_0(k',0)\bar{a}_0(k',0)$$
$$a_0''\bar{a}_0'' = a_0(k'',0)\bar{a}_0(k'',0)$$

From here, the general solution to the $\varepsilon^0$ equation (Eq. (25)) is considered with the new found results for $a_0(k^*,\tau_2)$ and $\bar{a}_0(k^*,\tau_2)$,

$$a_0(k^*,\tau_2) = a_0(k^*,0)e^{i\beta(k^*)\tau_2}$$
$$\bar{a}_0(k^*,\tau_2) = \bar{a}_0(k^*,0)e^{-i\beta(k^*)\tau_2}$$

Equation (25) is written as follows:

$$A_0(k^*,\tau_0,\tau_2) = a_0(k^*,\tau_2)e^{i\omega_0^*\tau_0} + \bar{a}_0(k^*,\tau_2)e^{-i\omega_0^*\tau_0}$$

Utilizing the new found results for $a_0(k^*,\tau_2)$ and $\bar{a}_0(k^*,\tau_2)$, one arrives at the following expression:

$$A_0(k^*,\tau_0,\tau_2) = a_0(k^*,0)e^{i\left(\omega_0^*\tau_0+\beta(k^*)\tau_2\right)} + \bar{a}_0(k^*,0)e^{-i\left(\omega_0^*\tau_0+\beta(k^*)\tau_2\right)}$$

Writing the above expression strictly in terms of $\tau_0$, where $\tau_2 = \varepsilon^2\tau_0$, gives the following representation for $A_0(k^*,\tau_0)$:

$$A_0(k^*,\tau_0) = a_0(k^*,0)e^{i\left(\omega_0^*\tau_0+\varepsilon^2\beta(k^*)\tau_0\right)} + \bar{a}_0(k^*,0)e^{-i\left(\omega_0^*\tau_0+\varepsilon^2\beta(k^*)\tau_0\right)}$$

$\beta^*$ is expressed in terms of its real and imaginary parts to yield the final representation for $A_0(k^*,\tau_0)$,

$$\begin{aligned}\beta(k^*) &= \Delta_{k^*} + i\Gamma_{k^*}\\ A_0(k^*,\tau_0) &= a_0(k^*,0)e^{i\left(\omega_0^*\tau_0+\varepsilon^2(\Delta_{k^*}+i\Gamma_{k^*})\tau_0\right)}\\ &\quad + \bar{a}_0(k^*,0)e^{-i\left(\omega_0^*\tau_0+\varepsilon^2(\Delta_{k^*}+i\Gamma_{k^*})\tau_0\right)}\\ A_0(k^*,\tau_0) &= a_0(k^*,0)e^{i\left(\left(\omega_0^*+\varepsilon^2\Delta_{k^*}\right)\tau_0\right)}e^{-\varepsilon^2\Gamma_{k^*}\tau_0}\\ &\quad + \bar{a}_0(k^*,0)e^{-i\left(\left(\omega_0^*+\varepsilon^2\Delta_{k^*}\right)\tau_0\right)}e^{\varepsilon^2\Gamma_{k^*}\tau_0}\end{aligned} \tag{37}$$

Three-wave interaction leads therefore to an additional frequency shift proportional to the square of the strength of the nonlinearity. Moreover, three-wave interaction leads to a damping of each wave, that is, a finite phonon-mode lifetime. This result is the classical mechanics equivalent of that reported within the framework of quantum mechanics [1–3,6].

## 3 Numerical Analysis of 1D Anharmonic Monoatomic Crystal

**3.1 Molecular Dynamics and Spectral Energy Density Analyses.** In this section, we shed additional light on three phonon-scattering processes in one-dimensional anharmonic crystals using the numerical method of MD. To accurately model an infinite crystal with a finite MD simulation cell, periodic boundary conditions (PBCs) are utilized. PBCs suppress modes of vibration with wavelength longer than the MD simulation cell length, leading to a discrete set of phonon modes. This is easily seen by considering a 1D monoatomic system composed of N atoms interacting via a nearest neighbor harmonic (or anharmonic) potential. In this case, imposing PBCs leads to atom N interacting with atom 1, thus forming a ring. Modes with wavelengths exceeding the length $L = Na$, where $a$ is the interatomic spacing, are not compatible with the constraint of the ring geometry and cannot be supported by that structure. The finite number of phonon modes will also impact the number of three-phonon interactions that may take place in a finite simulation cell. The discrete phonon modes may not allow the requirement of frequency conservation. These points will be illustrated with numerical simulations of the 1D anharmonic monoatomic crystal (Sec. 3.2).

For the present discussion, the equation of motion (Eq. (1)) is integrated by MD techniques with PBCs using the velocity Verlet algorithm under the microcanonical ensemble (constant energy) [18]. This scheme ensures energy is conserved within 0.5%. Harmonic MD simulations of the 1D monoatomic crystal utilize $\beta = 1.0$ N/m and $\varepsilon = 0.0$ N/m$^2$, whereas anharmonic simulations utilize $\beta = 1.0$ N/m and $\varepsilon = [0.9–3.7]$ N/m$^2$. The 1D crystal consists of a chain of 1.0-kg masses spaced periodically 1.0 m apart. These parameters can be easily scaled down to represent an atomic system. To initiate a simulation, every mass in the MD simulation cell is randomly displaced from its equilibrium position. The maximum value in which a mass can be displaced is constrained such that instabilities do not emerge in the potential energy function. MD simulations are run for $2^{21}$ time steps with a timestep of 0.01 seconds. For postprocessing spectral energy density (SED) calculations, velocity data is collected for each mass in the simulation cell over the entire simulation time.

The SED method is a technique for predicting phonon dispersion relations and lifetimes from the atomic velocities of the particles in a crystal generated by classical MD [19]. The SED method offers a comprehensive description of phonon properties, because individual phonon modes can be isolated for analysis, and is computationally affordable for the systems that will be examined in this section. Formally, the expression for SED is written as follows:

$$\Phi\left(\vec{k},\omega\right) = \frac{1}{4\pi\tau_0 N}\sum_{\alpha}\sum_{b}^{B} m_b \left|\int_0^{\tau_0}\sum_{n_{x,y,z}}^{N} v_\alpha\left(\begin{matrix}n_{x,y,z}\\ b\end{matrix};t\right)\times e^{\left(i\vec{k}\cdot\vec{r}_0-i\omega t\right)}dt\right|^2$$

where $\tau_0$ represents the length of time over which velocity data is collected from a given MD simulation, $N$ is the total number of unit cells represented in the MD simulation, and $v_\alpha\left(\begin{smallmatrix}n_{x,y,z}\\ b\end{smallmatrix};t\right)$ represents the velocity of atom b (of mass $m_b$ in unit cell $n_{x,y,z}$) in the $\alpha$ direction. For a specified wave vector $(\vec{k})$, the spectrum relating SED to frequency is found by adding the square of the absolute value of the Fourier transform of the discrete temporal signal

$$f(t) = \sum_{n_{x,y,z}}^{N_T} v_\alpha\left(\begin{matrix}n_{x,y,z}\\ b\end{matrix};t\right)\times e^{\left(i\vec{k}\cdot\vec{r}_0\right)}$$

for every [$\alpha$, $b$] pair. A SED value represents the average kinetic energy per unit cell as a function of wave vector and frequency. A peak in the spectrum relating SED to frequency signifies a vibrational eigenmode for wave vector $(\vec{k})$. The shape of the frequency spread for eigenmode $(\vec{k})$ is represented with the Lorentzian function,

$$\Phi\left(\vec{k},\omega\right) = \frac{1}{1+\left[(\omega-\omega_c)/\gamma\right]^2}$$

where $I$ is the peak magnitude, $\omega_c$ is the frequency at the center of the peak, and $\gamma$ is the half-width at half-maximum. The lifetime for phonon mode $(\vec{k})$ is given as $\tau = 1/2\gamma$ [19]. Nondegenerate wave vector modes are dependent on the size of the MD simulation cell and are written as follows: $k_i = 2\pi n_i/aN_i$, where $a$ is the lattice constant, $N_i$ is the total number of unit cells in the $i$ direction, and $n_i$ is an integer ranging from $-N_i+1$ to $N_i$. The SED method is subsequently used to render phonon band structures for several configurations of the 1D anharmonic crystal.

**3.2 One-Dimensional Anharmonic Monoatomic Crystal.** To begin with, the band structure generated by the SED method is shown for the 1D harmonic monoatomic crystal (Fig. 2). Figure 2 shows contours of constant SED over the wave vector-frequency plane. There are 101 discrete, nondegenerate wave vectors

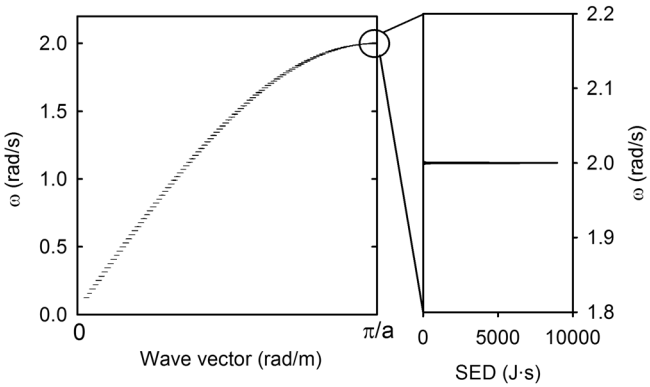


**Fig. 2 (Left) Band structure of 1D harmonic monoatomic crystal. (Right) SED-frequency plot showing wave vector mode $k = \pi/a$.**

resolved between the center of the irreducible Brillouin zone and the zone edge at $k = \pi/a$. In the band structure, there is a nearly linear region that accounts for the characteristics of long wavelength excitations in the 1D harmonic crystal. At larger wave vector values, a departure from the linear behavior is apparent and the phase velocity of phonon modes is markedly different from the group velocity. This is similar to the expected dispersion behavior of the infinite monoatomic harmonic crystal. At the edge of the irreducible Brillouin zone, a SED-frequency plot is reported. A peak in the spectrum shows this vibrational mode contributing significantly to the average kinetic energy per unit cell. A Lorentzian function is fit to this peak and shows a finite value for half-width at half-maximum ($\gamma$), because the fast Fourier transform scheme used in the SED calculation involves a signal sampled over a finite time window. This value for half-width at half-maximum is subsequently used as a lower bound for the error on lifetime estimated with the SED method. This error amounts to one interval in the discrete frequency scale. The band structure of the harmonic system is highlighted in the long wavelength regime; Fig. 3 zooms in on a region of the dispersion curve near $k = \pi/10a$. In Fig. 3, on the right-hand side, four SED-frequency plots are shown (plots a–d). Each plot represents a different MD simulation of the 1D harmonic monoatomic crystal. Each MD simulation begins with a random starting configuration for atomic displacements in the 1D crystal. It is observable from these four plots that, for a given wave vector, the SED takes on different values. This is due to the fact that, in a harmonic crystal, energy contained within a particular mode cannot be passed to other modes of vibration. This highlights the sensitivity of the vibrational

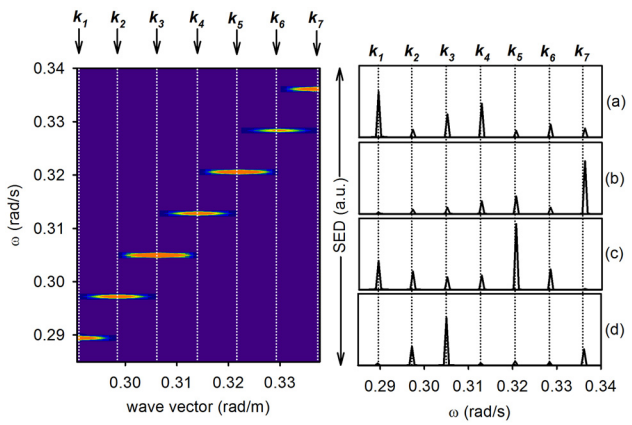


**Fig. 3 (Left) Band structure (constant SED contours) for 1D harmonic monoatomic crystal near $k = \pi/10\,a$. (Right) SED-frequency plots for four MD simulations differing in their initial random configurations.**

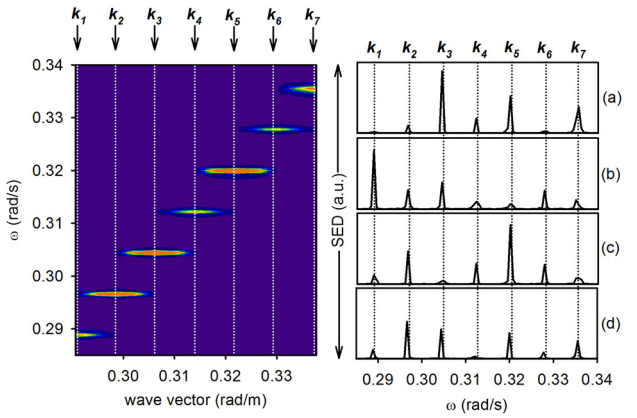


**Fig. 4 (Left) Band structure (constant SED contours) for 1D anharmonic monoatomic crystal near $k = \pi/10a$. (Right) SED-frequency plots for four MD simulations differing in their initial random configurations.**

modes of the harmonic crystal on the initial configuration. Consequently, to obtain a nonbiased band structure, multiple MD simulations must be run such that an average can be taken of the different SED values for each discrete, nondegenerate wave vector mode. An average of plots (a–d) is shown on the left-hand side of Fig. 3, with the color of the contours signifying SED intensity. A Lorentzian function is fit to each of the peaks in the left-hand figure and shows the same value for half-width at half-maximum as that calculated in Fig. 2. For comparison, the band structure of the 1D anharmonic monoatomic crystal near $k = \pi/10a$ is shown in Fig. 4. Here, the parameter characterizing the degree of anharmonicity in the 1D crystal is $\varepsilon = 3.0$ (see Fig. 1(*b*)). Similarly to Fig. 3, the four plots on the right-hand side of Fig. 4 represent SED-frequency plots generated from four different MD simulations. The SED intensity for a given mode varies from simulation to simulation, which indicates that energy does not easily exchange between modes of vibration in the 1D anharmonic crystal. In contrast to the purely harmonic system, there are some peaks in the SED-frequency spectra that show slightly larger values for half-width at half-maximum. However, it is critical that averages be taken for SED data extracted from several MD simulations such that an accurate quantification of phonon lifetime can be realized. The contour map on the left-hand side of Fig. 4 represents an average over plots (a–d). Lorentzian functions are fit to the peaks in this figure. The half-width at half-maximum for all peaks is found to be comparable to the harmonic case. With a random initial displacement of the masses of at most 10% of the lattice spacing "a," the total energy of the anharmonic system is only 1.3% higher than that of the harmonic system. Under this condition, the system can be considered to be weakly anharmonic and second order perturbation theory is applicable. The system studied here belongs to the category of weak coupling and is not expected to behave like the Fermi–Pasta–Ulam model, where strong nonlinearity leads to persistent recurring vibrational modes [20]. Considering the final expression for $A_0(k^*, \tau_0)$ in Sec. 2.2 (Eq. (37)), which represents the 0th order term in the asymptotic expansion of $A(k^*, \tau)$, describing three-wave interactions, $\Gamma_{k^*}$ (Eq. (36)) corresponds to a decay constant for mode $k^*$. Half-width at half-maximum calculations of peaks in SED-frequency spectra embody $\Gamma_{k^*}$. In the long wavelength regime, $\Gamma_{k^*}$ is small because of squared sinusoidal terms inside the double summation over $k'$ and $k''$. Accordingly, one should not expect large values for half-width at half-maximum in the long wavelength limit. The complete band structure for the 1D anharmonic monoatomic crystal is shown in Fig. 5. The band structure is generated from SED averages taken from four MD simulations. In Fig. 5, it seems that each nondegenerate wave vector is associated with multiple eigenfrequencies, due to the fact that multiple peaks appear in the SED. At the edge of the

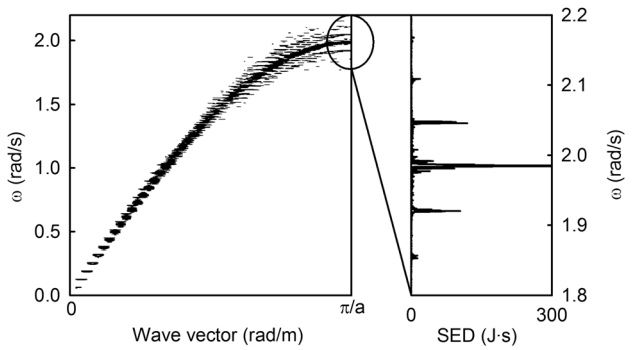


**Fig. 5 (Left) Band structure for 1D anharmonic monoatomic crystal. (Right) SED-frequency plot showing wave vector mode $k = \pi/a$. $\varepsilon = 3.0$ and initial random displacement does not exceed 10% of $a$.**

irreducible Brillouin zone, an intense central peak is seen along with multiple, less intense symmetrical satellite peaks. These satellite peaks emerge when the anharmonicity of the system is adequately sampled (i.e., large amplitudes of vibration). Equation (29) of Sec. 2.2 is utilized to explain the appearance of these satellite peaks. This equation represents the first order term in the asymptotic expansion of $A(k^*, \tau)$, describing three-wave interactions. Inside the double summation over $(k', k'')$ in Eq. (29), conservation of wave vectors is imposed: $\delta_{k'+k'',k^*} \rightarrow k' + k'' = k^*$. If the mode of interest is $k^* = \pi/a$, then conservation of wave vector can be satisfied by adding nondegenerate wave vector pairs that yield $k^*$. With $N = 400$, nondegenerate wave vectors are limited to the following:

$$k_i = \frac{n_i}{400} \cdot \frac{2\pi}{a}$$

If only wave vectors contained between the center of the irreducible Brillouin zone and the zone edge are considered, then $n_i$ ranges from 0 to 200. As a first example, to satisfy wave vector conservation, consider two wave vectors: (1) the first nondegenerate wave vector before the zone edge at $(k = \pi/a)$ and (2) the first nondegenerate wave vector after the center of the irreducible Brillouin zone at $(k = 0)$. This pair of wave vectors is shown as Case I and satisfies wave vector conservation

$$\text{(Case I) } k' = \frac{199}{400} \cdot \frac{2\pi}{a}, \quad k'' = \frac{1}{400} \cdot \frac{2\pi}{a}, \quad \text{and} \quad k^* = \frac{200}{400} \cdot \frac{2\pi}{a}$$

As a second example, consider (1) the second nondegenerate wave vector before the zone edge at $(k = \pi/a)$ and (2) the second nondegenerate wave vector after the center of the irreducible Brillouin zone at $(k = 0)$. This pair of wave vectors is defined as Case II and satisfies wave vector conservation

$$\text{(Case II) } k' = \frac{198}{400} \cdot \frac{2\pi}{a}, \quad k'' = \frac{2}{400} \cdot \frac{2\pi}{a}, \quad \text{and} \quad k^* = \frac{200}{400} \cdot \frac{2\pi}{a}$$

We note that both cases do not conserve frequency. In both cases, since the dispersion relationship for the 1D anharmonic monoatomic crystal is not strictly linear, the frequency of mode $k'$ plus (or minus) the frequency of mode $k''$ will not exactly equal the frequency of mode $k^*$. Instead, the addition (or subtraction) of the frequencies associated with modes $k'$ and $k''$ will be slightly greater than (or less than) the frequency of mode $k^*$. This forces the denominator of the pre-exponential factors in Eq. (29) to become small, thereby contributing to a large value of $A_1(k^*, \tau_0, \tau_2)$. The presence of nonzero $A_1(k^*, \tau_0, \tau_2)$ indicates that discrete, near-resonance modes are initiated for short wavelength phonons $(k')$, interacting with long wavelength phonons $(k'')$. On the left-hand side of Fig. 6, we show nondegenerate wave vector modes $k'$ and $k''$, corresponding to Case I (top) and Case II (bottom). On the right-hand side, Fig. 6 shows the modes at $k^* = \pi/a$. In this image, the satellite peaks coincide with discrete, near-resonance modes. The central peak frequencies of modes $k'$ and $k''$ add (or subtract) to yield satellite peaks to the central peak for $k^* = \pi/a$. The primary satellite peaks at 1.999 and 1.969 rad/s come from Case I. The secondary satellite peaks at 2.015 and 1.951 rad/s come from Case II. Tertiary, quaternary, and other higher order satellite peaks exist and are revealed if the scale on the right-hand SED plot were adjusted. The magnitude of the satellite peaks depends upon the "distance" from the central peak at $k = \pi/a$, in accordance with their near-resonant character. This distance depends upon the size of the MD simulation. For an MD simulation with $N = 100$ atoms, there are 51 discrete, nondegenerate wave vector modes available between the center of the irreducible Brillouin zone and the zone edge. For $N = 1000$ atoms, there are 501 available modes. The resolution in wave vector space is finer for larger MD systems, as is the resolution in

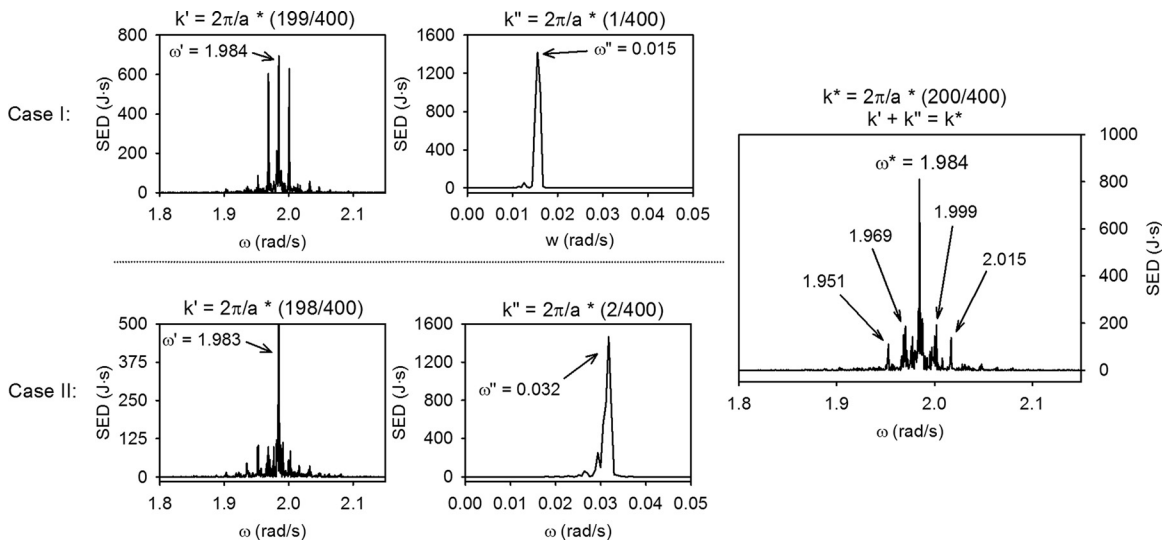


**Fig. 6 (Top, left) SED-frequency plots for wave vector modes $k'$ and $k''$, corresponding to Case I. (Bottom, left) SED-frequency plots for wave vector modes $k'$ and $k''$, corresponding to Case II. (Right) SED-frequency plot corresponding to $k^* = \pi/a$. For Cases I and II, wave vectors $k'$ and $k''$ satisfy wave vector conservation for mode $k^*$. The frequencies of modes $k'$ and $k''$ add (or subtract) to yield near-resonance peaks near $\omega^*(k^*)$.**

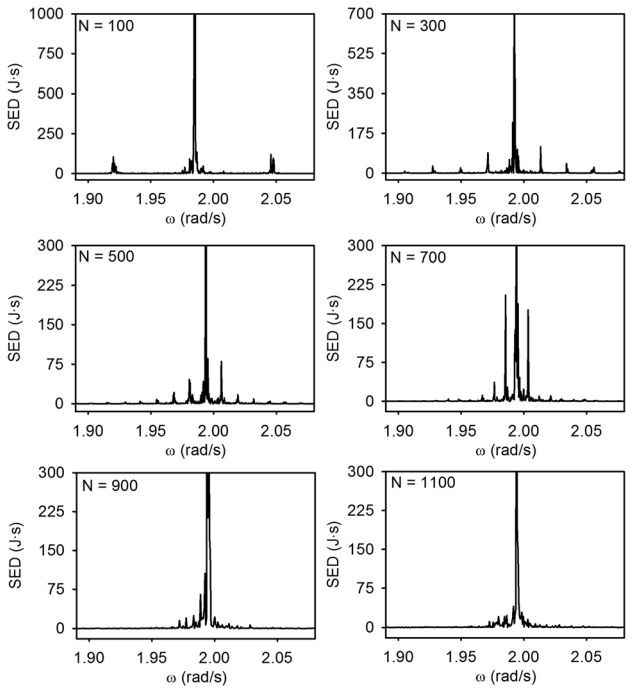


**Fig. 7 SED-frequency plots for 1D anharmonic monoatomic crystal at $k = \pi/a$ for MD systems of varying sizes. The parameter characterizing the degree of anharmonicity in the 1D crystal is $\varepsilon = 3.0$.**

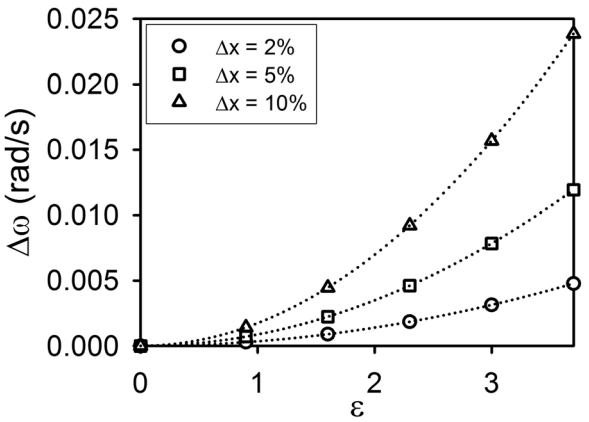


**Fig. 8 Frequency-shift evaluated at $k = \pi/a$ for 1D anharmonic crystal relative to harmonic case. Symbols represent different magnitudes for the maximum initial random displacement imposed upon the masses in the 1D crystal in terms of percentage of the lattice spacing. Circle, square, and triangle symbols represent small, intermediate, and large initial displacements, respectively.**

frequency space. Higher frequency resolution results in smaller spacing between satellite peaks. This is shown in Fig. 7. As the number of atoms (N) increases, the satellite peaks congregate around the central peak and increase in relative amplitude. In the limit of an infinite system, all satellite peaks merge into the central peak. For a phonon mode to decay, wave vector and frequency conservation rules must be satisfied. For short-wavelength phonon modes, these constraints are pathologically difficult to satisfy, because the monoatomic dispersion curve is not linear. The central frequency peaks in Fig. 7 represent the resonance mode of wave vector $k = \pi/a$. The satellite peaks in Fig. 7 represent frequency-nonconserving, near-resonance modes spawned from nonlinear wave interactions between short wavelength phonons and long-wave length phonons. The lifetime of phonon mode $k = \pi/a$ comes from fitting a Lorentzian function to the central peak. As Fig. 7 shows, the half-width at half-maximum for phonon mode $k = \pi/a$ is rather insensitive to the number of atoms in the MD simulation cell. It is found that the half-width at half-maximum for $k = \pi/a$ is the same order of magnitude as the error estimate found from the harmonic case in Fig. 2. As a result, lifetime of high-frequency phonon modes in the anharmonic monoatomic crystal is inherently long, because wave vector and frequency conservation constraints cannot be satisfied.

In comparing the anharmonic band structure with the harmonic band structure at $(k = \pi/a)$, there is an obvious shift in frequency of the central peak. The perturbation analysis of the single-wave dispersion has shown that the anharmonic dispersion curve is frequency-shifted (with respect to the harmonic dispersion curve) by a quantity that has quadratic dependence on the strength of the nonlinearity parameter $\varepsilon$. Figure 8 shows a plot mapping the frequency shift relative to the harmonic system for several values of $\varepsilon$ for a MD simulation cell consisting of $N = 200$ atoms. In Fig. 8, three different curves are rendered. Each curve represents a different magnitude for the initial random displacement imposed upon the masses in the 1D crystal in terms of percentage lattice spacing. The magnitude of the initial displacement controls the amplitude of the phonon modes. For triangles, the maximum value a mass can be displaced is 10% of the lattice spacing. For squares and circles, displacement values are 5% and 2%, respectively. Quadratic dependence is observed for values of $\varepsilon$ ranging from 0.0 to 3.7. Beyond $\varepsilon = 3.7$, the potential energy function becomes completely unstable. Perturbation analysis of the weakly anharmonic 1D monoatomic crystal has shown that, in the long-wavelength regime, phonon lifetime is inherently long, because of $\Gamma_{k^*}$ in Eq. (36). Analysis of the weakly anharmonic 1D monoatomic crystal has shown that, in the short-wavelength regime, the lifetime of phonon modes is not significantly affected by nonlinear interaction forces, because it is pathologically difficult to satisfy the conditions for frequency and wave vector conservation. In the short-wavelength regime, there do, however, exist conditions between short-wavelength phonons and long-wavelength phonons, whereby near-resonance peaks emerge in plots of SED-frequency spectra. Satellite peaks materialize when the anharmonicity of the system is adequately sampled. Lastly, nonlinear interaction forces lead to amplitude-dependent frequency shifts.

**3.3 Anharmonic One-Dimensional Superlattices.** In this section, the insight gained from analysis of the 1D harmonic and anharmonic crystals is extended to a series of superlattice configurations. A characteristic feature offered by periodic media is folded phononic band structures. Band-folding allows the conditions for wave vector and frequency conservation to be easily satisfied, thereby greatly impacting three phonon processes, because a greater number of phonon mode decay channels are available. Three direct consequences of band folding are (1) modulated eigenfrequencies for vibrational modes, (2) decreased phonon mode group velocities, and (3) altered phonon mode lifetimes. The superlattice configurations considered in this section do not possess the ability to boundary-scatter phonons, because the potential describing the interaction between particles of differing mass is identical to the potential between particles of the same mass. Accordingly, the discussion of phonon mode lifetime is limited to coherent, band-folding effects. The main objective in this section is to illustrate the role superlattice periodicity plays in modulating eigenfrequencies and phonon mode lifetimes at a constant filling fraction. For all superlattices, the highest frequency phonon mode at the center of the irreducible Brillouin zone will be considered. The total number of atoms simulated with MD is $N = 800$. Every plot presented represents an average over a minimum of five unique MD simulations with randomly generated initial conditions. For superlattice unit cells, the mass of the black atom amounts to 50% of that of the white atom.

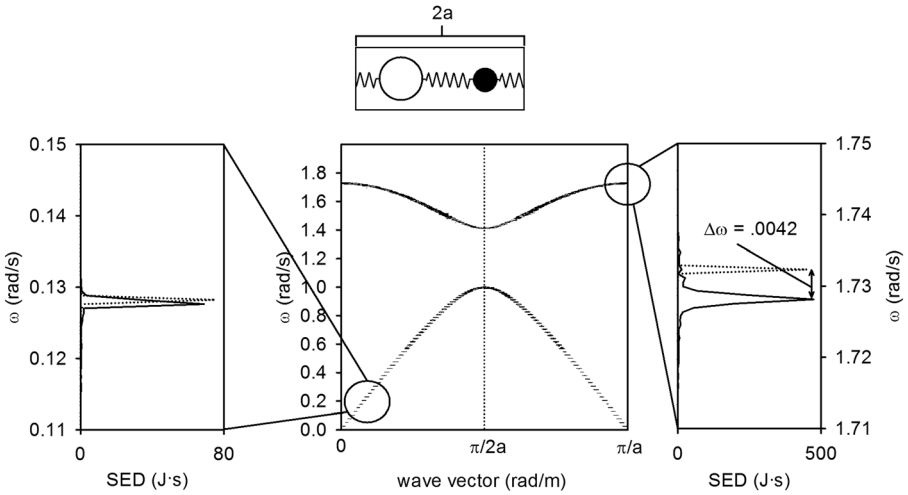


**Fig. 9 (Top) Unit cell for diatomic crystal. (Center) Band structure for 1D anharmonic diatomic crystal. (Left) SED-frequency plot at $k = \pi/20a$ with peaks for harmonic (dashed line) and anharmonic (solid line) cases. (Right) SED-frequency plot at $k = \pi/a$ with peaks for harmonic (dashed line) and anharmonic (solid line) cases.**

To begin with, consider the 1D anharmonic diatomic crystal (superlattice 1:1), as pictured in Fig. 9. In comparison to the 1D anharmonic monoatomic crystal, a single fold in the phononic band structure occurs at wave vector mode $= \pi/2a$. Similarly to the monoatomic case, there is a region in the band structure where frequency varies linearly with wave vector. In Fig. 9 (right), a SED-frequency plot is highlighted at $k = \pi/a$. This mode, minus a reciprocal space vector, is identical to the mode at the center of the irreducible Brillouin zone and coincides with a group velocity value of zero. Two peaks are visible in this plot: the dashed line represents a peak for the 1D harmonic diatomic crystal, whereas the solid line represents the anharmonic case. There is a noticeable frequency shift as well as a marked difference in peak breadth. Peak broadening is directly associated with satisfaction of conservation of wave vector and frequency conditions; the folded band in the band structure allows these conditions to be met more easily. In the left-hand plot of Fig. 9, two peaks are apparent. The dashed line corresponds to the diatomic harmonic system, and the solid line represents the anharmonic case. There appears to be no significant difference in peak position or width. This result was seen in the anharmonic monoatomic case for long-wavelength, low-frequency wave vector modes.

Larger superlattice configurations are now considered to probe the impact superlattice periodicity has on frequency shift and phonon lifetime. In Fig. 10, the band structure for a superlattice configuration consisting of a unit cell comprised of two heavy atoms and two light atoms (superlattice 2:2) is displayed. Four distinct bands span the irreducible Brillouin zone. The highest frequency band shows near-zero group velocity for all nondegenerate wave vector modes. A SED-frequency plot is highlighted at $k = \pi/2a$. This phonon mode coincides with a group velocity value of zero. This plot shows information for the harmonic (dashed line) and anharmonic (solid line) cases. Similar to Fig. 9, there is a noticeable shift in frequency and the anharmonic peak is significantly broader than the harmonic peak. In comparison to the diatomic case, the increased number of bands spanning the irreducible Brillouin zone allows the conditions for conservation of wave vector and frequency to be met with greater ease. That is, many more three-phonon processes satisfy those conditions. Accordingly, the anharmonic peak here shows greater width than the anharmonic peak in the right-hand plot of Fig. 9.

In Fig. 11, the band structure for a superlattice configuration comprised of eight atoms (superlattice 4:4) is displayed. Eight distinct bands span the irreducible Brillouin zone. Of these bands, several show wave vector modes with near-zero group velocity.

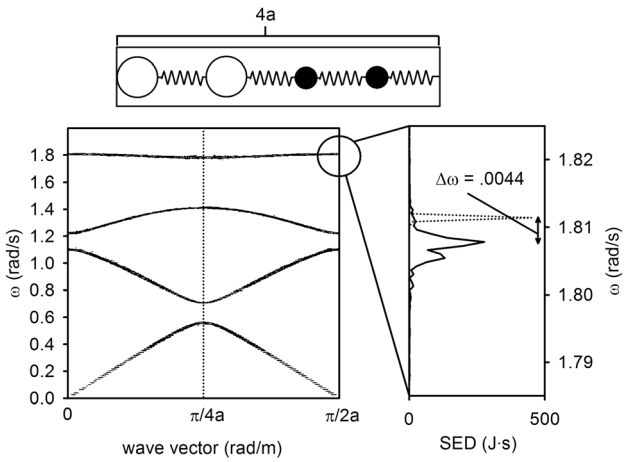


**Fig. 10 (Top) Four-atom unit cell. (Left) Anharmonic band structure corresponding to the four-atom unit cell. (Right) SED-frequency plot at $k = \pi/2a$. Dashed line represents the harmonic case, whereas the solid line represents the anharmonic case.**

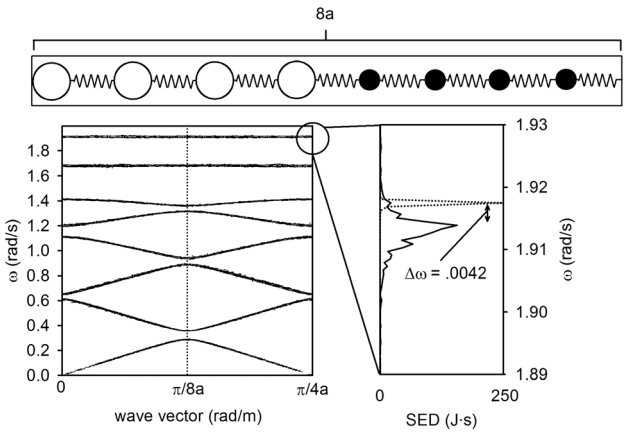


**Fig. 11 (Top) Eight-atom unit cell. (Left) Anharmonic band structure corresponding to the eight-atom unit cell. (Right) SED-frequency plot at $k = \pi/4a$. Dashed line represents the harmonic case, whereas the solid line represents the anharmonic case.**

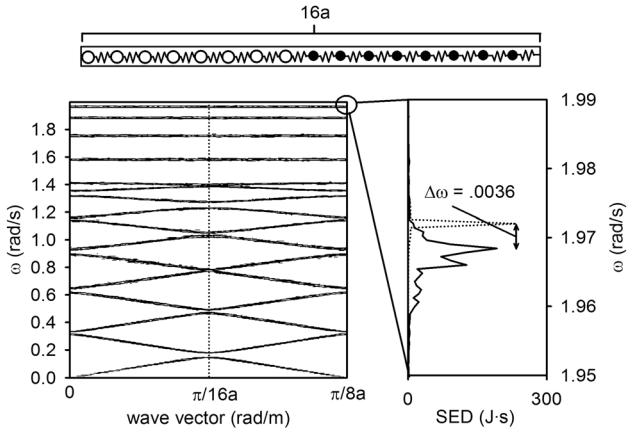


**Fig. 12 (Top) Sixteen-atom unit cell. (Left) Anharmonic band structure corresponding to the sixteen-atom unit cell. (Right) SED-frequency plot at $k = \pi/8a$. Dashed line represents the harmonic case, whereas the solid line represents the anharmonic case.**

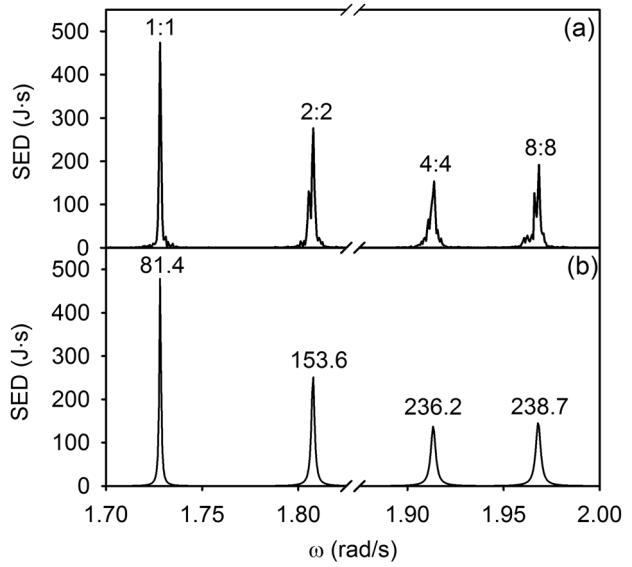


**Fig. 13 (*a*) (Left to right) 1:1, 2:2, 4:4, and 8:8 SED-frequency plot with peaks respectively corresponding to the superlattice configurations depicted in Figs. 9–12. (*b*) Lorentzian function fits to the SED-frequency spectra in (*a*). Lorentzian peaks are labeled with half-width at half-maximum values in units of $10^{-6}$ Hz.**

The SED-frequency plot on the right-hand side of Fig. 11 highlights phonon mode $= \pi/4a$. This mode associates with zero group velocity, and the SED-frequency plot shows a peak much broader than that seen in Figs. 9 and 10. It is apparent that anharmonic SED-frequency peaks broaden as the number of bands spanning the irreducible Brillouin zone increases. According to this, phonon mode lifetime is significantly reduced by the number of available bands. Since phonon mode group velocity is equal for all of the phonon modes studied in Figs. 9–11 (e.g., $v_g = 0$), lifetime reduction is attributed solely to superlattice size and band-folding effects. With this notion in mind, a final configuration is introduced (Fig. 12) with superlattice periodicity 16a (superlattice 8:8). Similar to Figs. 9–11, Fig. 12 shows a frequency shift and peak broadening for the highest frequency anharmonic mode at $k = \pi/8a$. To compare all four superlattice configurations, Fig. 13 shows (*a*) SED-frequency plots and (*b*) Lorentzian function fits to SED-frequency data corresponding to the mode with highest frequency. Qualitatively (in Fig. 13(*a*)) and quantitatively (in Fig. 13(*b*)), it is observable that, as the length of the period decreases, a general narrowing occurs for anharmonic SED-frequency peaks. Accordingly, phonon mode lifetime increases when the period of the superlattice is decreased. This observation is consistent with the work presented by Garg et al. [21]. In this study, it was shown that the thermal conductivity of a small period Si-Ge superlattice could be higher than that of the constituent materials. In that model, the authors calculated the thermal conductivity using the Boltzmann transport equation within the single-mode relaxation time approximation [22]. They modeled the superlattice with harmonic and anharmonic force constants derived from density-functional theory. In that work, the interfaces were treated as perfect (no boundary scattering). It was found that mass mismatch between Si and Ge atoms essentially controls phonon dispersion in the superlattices. The model also considered only three-phonon anharmonic scattering processes. Under these conditions, an increase in lifetime of the transverse acoustic (TA) modes (the majority contributors to thermal conductivity) was responsible for the observed increase in thermal conductivity of the short-period superlattice. This increase in lifetime was explained by the effect of a reduction in periodicity on the band structure of the superlattice that leads to bands that do not allow three-phonon scattering events involving TA modes that satisfy the wave vector and frequency conservation rules. Additional lengthening of the phonon lifetime (and increase in thermal conductivity) was further demonstrated by changing the mass mismatch between the constituent materials.

Other authors have addressed the issue of boundary scattering in superlattices; however, these investigations have included interfacial scattering phenomena (phonon mode boundary scattering) in addition to coherent band-folding effects. Experimentally and theoretically [23–25], it has been demonstrated that phonon-boundary collisions play a leading role in decreasing the lifetime of thermal phonons in semiconductor superlattice configurations.

## 4 Conclusions

Analysis of the weakly anharmonic 1D monoatomic crystal and several 1D superlattice configurations has revealed that phonon mode lifetime depends strongly on satisfaction of the conditions for wave vector and frequency conservation. It is realized that, by cleverly tailoring the band structure of a superlattice, the lifetime of specific phonon modes can be modulated. This notion has particular significance in engineering materials with exceptional thermal properties. Additionally, it was demonstrated for the anharmonic monoatomic crystal that there exist conditions between short- and long-wavelength phonons, whereby near-resonance satellite peaks emerge in SED-frequency plots. Future work is directed at analytically quantifying three-phonon processes in the anharmonic diatomic system via perturbation analysis. Additionally, it is of particular interest to quantify the effect boundary scattering has on the vibrational modes supported by the superlattice configurations.

## Acknowledgments

We gratefully acknowledge support from NSF grant No. 0924103.

## References

[1] Wallace, D. C., 1972, *Thermodynamics of Crystals*, 3rd ed., Wiley, New York, pp. 128.
[2] Wallace, D. C., 1966, "Renormalization and Statistical Mechanics in Many-Particle Systems. I. Hamiltonian Perturbation Method," Phys. Rev., **152**, pp. 247–260.
[3] Maradudin, A. A., and Fein, A. E., 1962, "Scattering of Neutrons by an Anharmonic Crystal," Phys. Rev., **128**, pp. 2589–2608.
[4] Kokkedee, J. J., 1962, "Anharmonic Effects in Coherent Scattering of Neutrons by Crystals—A Formal Treatment of Shift and Width of Peaks in Scattering Spectrum," Physica, **28**, pp. 374–408.
[5] Cowley, R. A., 1963, "The Lattice Dynamics of an Anharmonic Crystal," Adv. Phys., **12**, pp. 421–480.

[6] Khoo, I. C., and Wang, Y. K., 1976, "Multiple Time Scale Analysis of an Anharmonic Crystal," J. Math. Phys., **17**(2), pp. 222–227.
[7] Krylov, N. M., and Bogoliubov, N. N., 1947, *Introduction to Nonlinear Mechanics*, Princeton University, Princeton, NJ, p. 102.
[8] Hyldgaard, P., and Mahan, G. D., 1997, "Phonon Superlattice Transport," Phys. Rev. B, **56**(17), pp. 10754–10757.
[9] Chen, G., Tien, C. L., Wu, X., and Smith, J. S., 1994, "Thermal Diffusivity Measurement of GaAs/AlGaAs Thin-Film Structures," ASME J. Heat Transfer, **116**, pp. 325–331.
[10] Capinski, W. S., and Maris, H. J., 1996, "Thermal Conductivity of GaAs/AlAs Superlattices," Physica B, **219–220**, pp. 699–701.
[11] Landry, E. S., Hussein, M. I., and McGaughey, A. J. H., 2008, "Complex Superlattice Unit Cell Designs for Reduced Thermal Conductivity, Phys. Rev. B, **77**, p. 184302.
[12] McGaughey, A. J. H., Hussein, M. I., Landry, E. S., Kaviany, M., and Hulbert, G. M., 2006, "Phonon Band Structure and Thermal Transport Correlation in a Layered Diatomic Crystal," Phys. Rev. B, **74**, p. 104304.
[13] Gorishnyy, T., Ullal, C. K., Maldovan, M., Fytas, G., and Thomas, E. L., 2005, "Hypersonic Phononic Crystals," Phys. Rev. Lett., **94**, p. 115501.
[14] Gillet, J.-N., Chalopin, Y., and Volz, S., 2009, "Atomic-Scale Three-Dimensional Phononic Crystals With a Very Low Thermal Conductivity to Design Crystalline Thermoelectric Devices," ASME J. Heat Transfer, **131**, p. 043206.
[15] Davis, B. L., and Hussein, M. I., 2011, "Thermal Characterization of Nanoscale Phononic Crystals Using Supercell Lattice Dynamics," AIP Adv., **1**, p. 041701.
[16] Narisetti, R. K., Leamy, M. J., and Ruzzene, M., 2010, "A Perturbation Approach for Predicting Wave Propagation in One-Dimensional Nonlinear Periodic Structures," ASME J. Vibr. Acoust., **132**, p. 031001.
[17] Manktelow, K., Leamy, M. J., and Ruzzene, M., 2011, "Multiple Scales Analysis of Wave-Wave Interactions in a Cubically Nonlinear Monoatomic Chain," Nonlinear Dyn., **63**, pp. 193–203.
[18] Haile, J. M., 1992, *Molecular Dynamics Simulation: Elementary Methods*, Wiley-Interscience, New York, pp. 23.
[19] Thomas, J. A., Turney, J. E., Iutzi, R. M., Amon, C. H., and McGaughey, A. J. H., 2010, "Predicting Phonon Dispersion Relations and Lifetimes From the Spectral Energy Density," Phys. Rev. B, **81**, p. 081411.
[20] Berman, G. P., and Izraileva, F. M., 2005, "The Fermi-Pasta-Ulam Problem: Fifty Years of Progress," Chaos, **15**, p. 015104.
[21] Garg, J., Bonini, N., and Marzani, N., 2011, "High Thermal Conductivity in Short-Period Superlattice," Nano Lett., **11**, pp. 5135–5141.
[22] Ziman, J. M., 1960, *Electrons and Phonons*, Oxford University, London, pp. 103.
[23] Lee, S. M., Cahill, D. G., and Vekatasubramanian, R., 1997, "Thermal Conductivity of Si-Ge Superlattices," Appl. Phys. Lett., **70**, pp. 2957–2959.
[24] Capinski, W. S., Maris, H. J., Ruf, T., Cardona, M., Ploog, K., and Latzer, D. S., 1999, "Thermal-Conductivity Measurements of GaAs/AlAs Superlattices Using a Picoseconds Optical Pump-and-Probe Technique," Phys. Rev. B, **59**, pp. 8105–8113.
[25] Wang, Y., Xu, X., and Venkatasubramanian, R., 2008, "Reduction in Coherent Phonon Lifetime in $Bi_2Te_3/Sb_2Te_3$ Superlattices," Appl. Phys. Lett., **93**, p. 113114.